VTT Technical Research Centre of Finland

Micromechanical performance of high-density polyethylene

Balobanov, Viacheslav; Verho, Tuukka; Heino, Vuokko; Ronkainen, Helena; Pelto, Jani

Published in:
Polymer Testing

DOI:
10.1016/j.polymertesting.2020.106936

Published: 01/01/2021

Document Version
Publisher's final version

Polymer Testing 93 (2021) 106936

Contents lists available at ScienceDirect

Polymer Testing

journal homepage: http://www.elsevier.com/locate/polytest

Micromechanical performance of high-density polyethylene: Experimental and modeling approaches for HDPE and its alumina-nanocomposites

Viacheslav Balobanov *, Tuukka Verho, Vuokko Heino, Helena Ronkainen, Jani Pelto

VTT Technical Research Centre of Finland Ltd, P.O. Box 1000, 02044, VTT, Finland

ARTICLE INFO

Keywords:
Polyethylene
Nanocomposite
Scratch test
Visco-elasto-plasticity
Finite element analysis

ABSTRACT

The scratch resistance of polymers is important for numerous applications, as scratching can lead to degradation of surface properties and also represents an elementary process in abrasive wear. However, scratching of polymers is a complex process involving several modes of deformation, and theoretical understanding of it is incomplete. Numerical modeling is a potentially useful means towards a clearer picture of the scratching process, but the central role of tip-substrate contact and highly localized large deformations makes finite element analysis (FEA) challenging. Here, we take further the numerical approach by investigating a highly ductile semi-crystalline polymer by FEA and taking the inherent rate dependency of polymers into account by using an elasto-viscoplastic material model. Two γ-Al_2O_3 and f-Al_2O_3 HDPE nanocomposites, which have shown themselves to be suitable for tribological applications, are studied. We discussed the effect of nanofillers on the scratch behavior and highlight the significance of recovery properties, which still pose a challenge to numerical modeling.

1. Introduction

The scratch and wear behavior of polymers has been the topic of numerous studies due to the ubiquity of polymer materials in technology in many different roles from enclosures to machine parts [1,2]. Polyethylenes are a group of widely used semi-crystalline and ductile polymers that are known for their low sliding wear, especially in the case of ultra-high molecular weight polyethylene, which is used in joint implants. High density polyethylene (HDPE), in its turn, is appealing due to its lower melt viscosity and higher stiffness. However, the rather low yield strength of polyethylenes reduce their scratch hardness [3,4]. The scratch behavior of HDPE has been widely studied in several papers [5–7], and nano- or micronscale fillers are frequently added to achieve better wear and scratch resistance [8–15].

Recently, we studied the effect of four different types of nanoparticles (NPs) on the micromechanical properties, crystalline morphology, friction and wear resistance of high molecular weight HDPE. We found improvement in sliding and abrasive wear performance in the case of two nano-alumina fillers. The nanocomposites had significantly higher coefficient of friction against steel surface as compared to the neat reference HDPE. Moreover, it was discovered that the improvement in the wear properties was not linked to any dramatic morphology change of the polymer, nor the measured micro-indentation moduli, elastic or plastic work during the indentation test. In fact, enhanced wear resistance could be achieved with NPs having both positive or negative effect on the elastic modulus of HDPE composite. However, in contrast, it was perfectly in correlation with the improved thermomechanical properties (higher glass transition and melting temperatures), which is an indication that the NPs had changed the dynamics of the PE chains, that is viscoelasticity/plasticity on both the amorphous and crystalline phases. Furthermore, as a general rule, the HDPE nanocomposites have slightly reduced degree of crystallinity compared to the HDPE reference, which is logically reflected in the surface elasticity and indentation hardness of the material [16].

Earlier investigators have shown that surface modification of NPs has a specific role in the mechanical behavior of HDPE nanocomposites. For example, in Ref. [17] it is found that with silane coating on the Al_2O_3, a thinner coating layer seems to correlate with optimum particle dispersion but a thicker layer of longer grafted chains promotes particle-matrix bonding. Stress-induced cavitation on the interphase between LDPE and silane treated nano-Al_2O_3 was reported in Ref. [18]. Noteworthily, cavitation is typically associated with poor interfacial bonding in composites and a high plastic strain, and vice versa, lack of cavitation indicates good interfacial bonding. Previous investigations on LDPE

* Corresponding author.
E-mail address: viacheslav.balobanov@vtt.fi (V. Balobanov).

https://doi.org/10.1016/j.polymertesting.2020.106936
Received 6 June 2020; Received in revised form 23 October 2020; Accepted 24 October 2020
Available online 31 October 2020

nanocomposite have also highlighted the paramount role of the interface strength as dominant factor controlling the final polymer crystal nucleation and growth, such as the interference of the NPs on the formation of native polymer superstructures, (e.g. the crystalline/lamellae thickness, tie molecule density etc.) and also the resulting electrical and mechanical properties ([19–21]).

Adding the alumina NPs improves the friction and wear properties of HDPE making such a composite useful for tribological applications. Such materials have use in unlubricated sliding and possibly high abrasive conditions, such as in conveyor lines, wear strips, gears, piston, valves, etc. The properties of the studied injection moulded HDPE nanocomposites approached the properties of the state-of-the-art material compression moulded UHMWPE, and the materials have similar potential technical application as UHMWPE [22].

A systematic improvement of the scratch and abrasion properties of a polymer require a good understanding of the scratch process, i.e. the indentation and sliding with a single asperity. However, scratching of polymers is inherently complicated and involves viscoelastic and viscoplastic rate dependency, thermal effects and several damage modes depending on the scratch conditions. For detailed information on the localized deformation and failure processes, numerical modeling is needed. Early FEA studies investigated the scratching of generic elastoplastic materials with a conical indenter, studying the effect of parameters like material elasticity, friction and indenter cone angle [23–25]. It was found that the parameter previously used to characterize indentation conditions $X = \varepsilon_{el}/\tan(\alpha)$, where ε_{el} is elastic strain after yielding and α is the cone half angle, characterizes well the relative contributions of plasticity and elasticity and the "severity" of the scratching. Later studies by Hossain et al. [26–28], Jiang et al. [29, 30] and Pelletier et al. [31–34] are focused on qualitative predictions on the scratching of glassy polymers with accurate hardening curves and spherical indenters. However, the rate dependency of polymers has generally been omitted in the material models, with the exception of Aleksy, Kermouche and coworkers who studied the rate dependency of the scratch behavior of PMMA with a viscoelastic-viscoplastic rheological model [35,36]. Furthermore, quantitative numerical scratch studies of highly ductile polymers such as high molecular weight HDPE do not exist in the literature, to the best of our knowledge.

In this paper, we present a combined experimental and numerical study of the scratch behavior of HDPE. We investigate the effect of the tip speed and applied load, and study how the addition of Al_2O_3 NPs affects the behavior. In FEA, we adopt a recently published rheological model [37] for polyethylene with rate dependent yield and network hardening, and tackle the issue of high shear deformations under tip-substrate contact. We compare the experiments and simulations in both the scratch process itself (penetration and frictional force) and the post-scratch behavior (relaxation and recovery).

2. Experimental methods

2.1. Samples preparation and materials

In this study, commercially available high molecular weight HDPE (HE 1878E, Borealis) polymer was processed in-house pre-mixing mechanically with coupling agent and dispersion aid vinyltrimethoxy silane (purity 97%, Sigma-Aldrich) and other additives (antioxidants, stabilizers, etc.) prior to twin screw compounding. More details about the exact procedure and the recipes can be found in Ref. [16]. Two HDPE-based composites were processed similarly but with addition of 6 wt percent (wt-%) filler powders and additives required for better adhesion between the NPs and the neat polymer. The first is gamma phase aluminium oxide (γ-Al_2O_3, catalog number 44757, Alfa-Aesar) being porous nanopowder with primary average particle size of 20 nm (BET surface area est. 130 m^2/g), and the second is fumed aluminium oxide (f-Al_2O_3) nanopowder Aeroxide ALU C 805 (Evonik), treated with octyl silane by the supplier, with estimated BET surface area of 100 m^2/g. The choice of 6 wt% fillers is based on our experience and aimed at significant changes in the micromechanical properties and improved wear properties of the composite, but without drastic changes in polymer crystallization, bulk mechanical properties and melt viscosity of the nanocomposites.

Batches of test material was produced with MC15 HT (Xplore Instruments BV) providing mixing volume of 15 cm^3. The melt viscosity was recorded during the mixing period. Mixing process was continued until the melt viscosity had been stabilized, which was used as an indicator for the completion of the dispersion process under the mixing conditions. Cylindrical test pins (length 16 mm, diameter 10 mm) was directly injection moulded using ThermoHaake Minijet pneumatic injection moulding machine.

Cross sections of the cylindrical test pins were made by cutting in half, casting in epoxy, and polishing for the indentation and scratch testing.

2.2. Scratch test

CSM Micro Combi Tester by Anton Paar was used for scratch testing neat HDPE polymer and HDPE composites with Al_2O_3 NPs in constant laboratory conditions of $22 \pm 1°C$ temperature and relative humidity of $50 \pm 5\%$. Scratching speed was kept constant during scratching with velocities of 0.4, 4 and 40 mm/min and the scratch length of 5 mm. All the scratches were oriented similarly in direction of cylindrical axis. Two constant load levels of 0.1 N and 0.2 N were used. The contact load of 30 mN was applied prior to scratching load. Rockwell C diamond indenter with radius of 20 μm and cone angle of 120° was used to scratch the polymer surface. Five repetitions, each on a fresh surface, were performed for each material, loading and scratching velocity.

During the scratching, frictional forces and penetration depths were recorded. Penetration depth recording was started when the set contact load was met. In order to establish some data over relaxation over time, 2-D profilometer Mitutoyo Formtracer (SV–C3100) was used to observe the valleys and the peaks of the scratch groove right after the scratch test (some minutes after), and also after 2 h and 48 h.

2.3. Microindentation

CSM Micro Combi Tester (Anton Paar) was also used to determine the indentation modulus and indentation hardness of the studied materials with Vickers tip. Measurements were done with maximum load of 200–220 mN and loading rate of 100 mN/min and 1000 mN/min at constant laboratory conditions of $22 \pm 1°C$ temperature and relative humidity of $50 \pm 5\%$. A dwell time of 120 s was used when maximum load was applied. Force sensor has a resolution of 6 μN and the depth sensor resolution of 0.03 nm. Indentation testing followed the guidelines of ISO-14577 standard. Indentation pattern consists of ten indentations per material and loading rate.

2.4. Tensile testing

Tensile testing was done with Instron 4505H2190 test equipment according to ISO 527–1 under constant laboratory conditions of $24 \pm 1°C$ temperature and relative humidity of $50 \pm 5\%$. Drawing speeds 1–10 mm/min were used during testing and strain was verified with video extensometer. A total of six specimens were used for tensile tests.

2.5. Electron microscopy

Material characterization was done with FEG-SEM Zeiss Ultra Plus with Thermo Scientific EDS from the bulk material but also the scratches were characterized from the scratch bottom and also cross-sectional samples were prepared to observe the material behavior underneath the scratch and the shoulder formation. For the composite material, especially, the filler dispersion underneath the scratch was of interest.

Specimens were carbon evaporated prior imaging.

FIB-SEM was used to produce 3D image of the neat polymer and the composite. FIB-SEM imaging was done for the bulk of neat HDPE and the composite, and also for the bottom and shoulder area of the scratch groove on the HDPE composite to observe the effects of deformation. The equipment used here was Zeiss Crossbeam 540 & Capella FIB column with EDAX EDS, WDS and EBSD detectors.

3. Numerical methods

3.1. Material models

In the current study, the constitutive model described in Ref. [37] was utilized for numerical simulations with the following modifications. First, the effects of temperature was not considered for simplicity, faster convergence, and to reduce the number of material parameters that need to be determined. Nevertheless, the authors are aware of the importance of such effects and leave them for the further studies. The second modification relates to the simplification of the Ree-Eyring model to include only one relaxation process, as the rate dependency of yielding in HDPE at room temperature is dominated by just one process [38]. With this, the rheological model of the material in use takes the form depicted in Fig. 1.

The rheological model consists of two parts: Part A describing the hyperelastic and viscoplastic behavior stemming from intermolecular interactions, and Part B representing the orientational hardening. Below one can find the brief description of the model, material parameters and their influence on the mechanical behavior. The detailed information about the mathematical model with physical justifications can be found in Refs. [37] and references therein.

The elastic response represented by the spring in Part A in Fig. 1 is defined by Hencky hyperelasticity characterized by a logarithmic strain measure:

$$\boldsymbol{\sigma}_A = 2\mu_A \frac{1}{J} \ln\left(\overline{\boldsymbol{V}}_A^e\right) \tag{3.1}$$

where $\boldsymbol{\sigma}_A$ is the Cauchy stress tensor associated with Part A of the rheological model, J is the Jacobian determinant of the deformation gradient tensor $J = \det(\boldsymbol{F})$. Notation $\overline{\boldsymbol{V}}_A^e$ denotes the elastic part of the isochoric left stretch tensor $\overline{\boldsymbol{V}} = \sqrt{\overline{\boldsymbol{B}}}$, and $\overline{\boldsymbol{B}}$ is the isochoric left Cauchy-Green deformation tensor, $\overline{\boldsymbol{B}} = J^{-2/3}\boldsymbol{B} = J^{-2/3}\boldsymbol{F}\cdot\boldsymbol{F}^T$. The Part A shear modulus, being the only required material parameter at this point, is denoted by μ_A. It affects, evidently, the elastic response of the material.

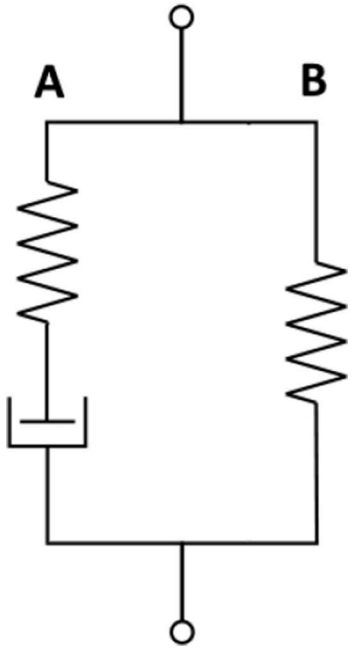

Fig. 1. Rheological model of the HDPE material.

A dash-pod in Part A denotes the viscoplastic response described by Eyring model, whereby the viscous stress $\boldsymbol{\sigma}_V$ is defined as follows:

$$\boldsymbol{\sigma}_V = \frac{k_B\theta}{V^*}\operatorname{arsinh}\left(\frac{\dot{p}}{\dot{p}^*}\exp\left(\frac{\Delta H}{R\theta}\right)\right) \tag{3.2}$$

where k_B and R stand for Boltzmann's constant and universal gas constant correspondingly, ΔH is the activation enthalpy and V^* is the activation volume, θ is the current temperature. Notation $\dot{p}$ designates the equivalent plastic strain rate, and $\dot{p}^*$ is the reference equivalent plastic strain rate, which, in general, depends on plastic deformation, but here this dependence is omitted for simplicity. As mentioned, temperature dependency is ignored in the current study and the temperature is assumed to be constant in the whole solution domain, $\theta = 298.15$ K. In view of this, the exponent in expression 3.2 is also a constant parameter depending on the activation enthaply ΔH. In the current consideration, its value is assumed to be equal to the reference value $\Delta H = 180$ kJ/mol and was not used as the model fitting parameter. That way, the following material parameters characterize viscoplastic behavior: the activation volume V^* and reference equivalent plastic strain rate in the plastically undeformed state $\dot{p}^*$. Both of them affect the yield stress and define the strain rate dependency.

The Part B spring signifies the orientational hardening of the material due to the alignment of the polymer chains. The so-called eight chain model is utilized to capture this behavior. Whereby, the Cauchy stress tensor associated with Part B is defined as

$$\boldsymbol{\sigma}_B = \frac{1}{J}\frac{\mu_B\lambda_{\text{lock}}}{3\lambda_c}\mathscr{L}^{-1}\left(\frac{\lambda_c}{\lambda_{\text{lock}}}\right)\overline{\boldsymbol{B}}' + \kappa\ln(J)\boldsymbol{I} \tag{3.3}$$

with the Part B shear modulus denoting by μ_B, bulk modulus κ, locking stretch λ_{lock}, average chain stretch $\lambda_c = \sqrt{\operatorname{tr}(\overline{\mathbf{B}})/3}$, $\overline{\boldsymbol{B}}' = \overline{\boldsymbol{B}} - \boldsymbol{I}\operatorname{tr}(\overline{\mathbf{B}})/3$ being the deviatoric part of $\overline{\boldsymbol{B}}$. Symbol $\mathscr{L}^{-1}$ stands for the inverse Langevin function $\mathscr{L}^{-1}(x) = 1/x - \coth x$, $\boldsymbol{I}$ is the second order identity tensor. Part B deformation process is characterized by the bulk modulus κ and second shear modulus μ_B, which define the material hardening behavior after alignment of polymer chains. Locking stretch λ_{lock}, in its turn, defines the threshold value of stretch which should be reached for hardening to be activated.

To determine the material parameters, we used the reference parameters for XLPE from Ref. [37] as the starting point and calibrate them with the aid of the experimental results from tensile tests (Fig. 2) and nano-indentation tests (Fig. 6 below). The estimation of Young's modulus $E = 620$ MPa was done by analysis of the linear elastic zone of the experimental curves in Fig. 2a. In literature, Poisson's ratio for high-density polyethylenes is usually assumed to be equal to $0.4 - 0.45$, and here we used the lower value of the range $\nu = 0.4$. With these two elastic parameters, we defined the total shear $\mu = \mu_A + \mu_B$ and bulk moduli κ.

In Fig. 2a, there is experimental data for tensile tests carried out with two loading rates. As one can observe, the transition to the plastic zone is not easily distinguishable and it is difficult to estimate the values of yield stresses. Nevertheless, the shift of the stress-strain curves due to strain rate dependency was utilized to define the activation volume V^* and $\dot{p}^*$. In addition, these material parameters was then fitted using the results of microindentation tests (Section 4.1). One can note that the experimental and numerical curves in Fig. 2a for the same rates do not coincide. The reason is that the experimental curves are measured by the experimental equipment for the large tensile specimens. In our experience, such data can be drastically different from the stress-strain state existing in the local point of the material, especially in the deep plastic

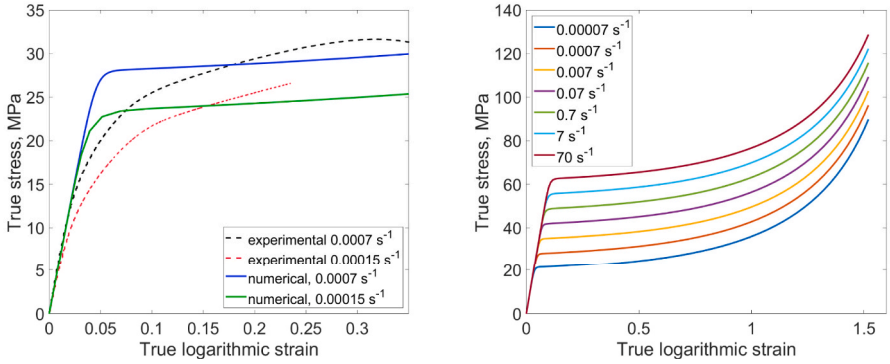

(a) Comparison of numerical and experimental data (b) Numerical model for different strain rates

Fig. 2. Experimental and numerical stress-strain curves of the HDPE polymer.

regime. Furthermore, it is different from the idealized numerical model. Therefore, the tensile test experimental data was mainly used for determining the elastic properties and estimation of the yield stresses.

The activation volume value is $V^* = 1.38$ nm^3, which is in the range of the values from literature. Thus, activation volume in Kanters et al. is 3.17 nm^3 [38], Hiss et al. get 1.52 nm^3 [39], Brown et al. get 2.51 nm^3 [40].

The final values of all the material properties are presented in Table 1. Fig. 2b represents the numerical tensile stress-strain curves for different loading rates demonstrating the strain rate sensitivity of the model.

3.2. Finite element analysis

3.2.1. Scratch tests

Numerical simulations were performed with the use of finite element software Abaqus. An Abaqus Fortran user material subroutine UMAT openly available as a supplement to Ref. [37] was adopted, after some minor changes, to model the material described in the previous section.

The solution domain is represented by a $0.60 \times 0.46 \times 1.60$ mm^3 brick sample of HDPE material and diamond conical indenter with conical angle of 120° and spherical 20 μm radius tip (Rockwell indenter). Note that only half of the actual domain was modeled and the symmetry boundary conditions were applied on the side along the scratch direction, see Fig. 3. Sides normal to the scratch direction were fixed, and vertical displacements were restricted on the bottom (boundary conditions were applied by analogy with [41]). The upper surface of the indenter was affected by concentrated vertical force F and velocity V applied in the scratch direction. In addition, the indenter was prevented from any rigid body rotations.

The size of the HDPE brick domain was chosen to be large enough to minimize the edge effect of boundary conditions. To ensure this, the sensitivity analysis has been performed meaning a number of scratch tests with various domain sizes, but preserving the other parameters (scratch length, loading, scratch velocity etc.).

The HDPE sample was meshed with linear brick elements with reduced integration and hourglass control. The mesh was preliminary locally refined in the scratch area (Fig. 4), and no local adaptive mesh refinement was adopted since it restricts the parallelisation of the solution process. Average characteristic size of the element in scratch area

Table 1
Material parameters values used for the numerical simulations.

μ_A[MPa]	V^*[nm^3]	$\dot{p}^*$[s^{-1}]	μ_B[MPa]	κ[MPa]	λ_{lock}	ΔH[kJ/mol]
219.43	1.38	4.6e+28	2.3	1033.3	3.71	180

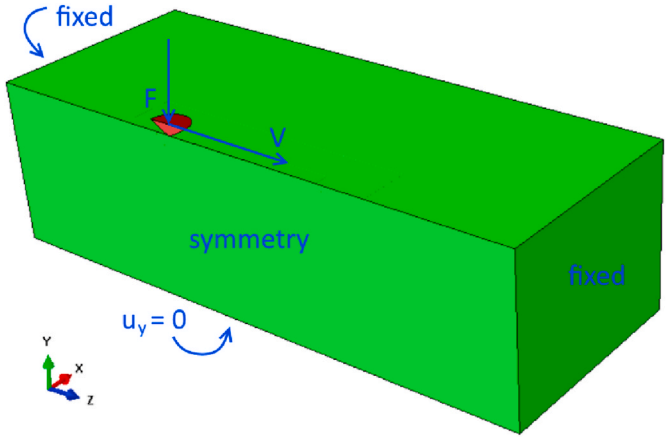

Fig. 3. Solution domain for scratch tests.

is 0.002 mm and up to 0.05 mm away from this area. Linear tetrahedral elements were utilized in a transition region from the smallest to largest brick elements. A convergence study has shown that the chosen mesh is fine enough since further refinement does not affect the results significantly. The indenter was meshed by quadratic tetrahedral elements.

In order to prevent convergence problems arising due to large local deformations concentrated in the contact area between indenter and the HDPE sample, the following actions were taken. First, the elements were elongated in vertical direction such that the aspect ratio is equal to 2:1:1. Second, the elements were initially distorted in the direction opposite to the scratch direction such that front and back faces of the elements make an angle of 45° with the planes of bottom and upper faces (see Fig. 4b).

Solution consisted of the four nonlinear quasi-static steps performed by the Abaqus/Standard solver. During the first step, the vertical displacement was applied to the indenter. During the second step, the indenter was affected by the vertical loading F and moved in scratch direction with velocity V. In the course of the third and fourth steps, the indenter moved out of the HDPE sample and subsequent relaxation process happened.

3.2.2. Indentation tests

The solution domain for the numerical Vickers indentation tests is represented by the $0.7 \times 0.7 \times 0.7$ mm^3 cubic sample of the HDPE material and Vickers pyramidal diamond indenter. Only quarter of the actual domain were modeled and symmetry boundary conditions were applied on two sides as depicted in Fig. 5a. The vertical displacements were restricted on the bottom side of the HDPE sample. As for the scratch tests domain described in section 3.2.1, the sensitivity tests have been

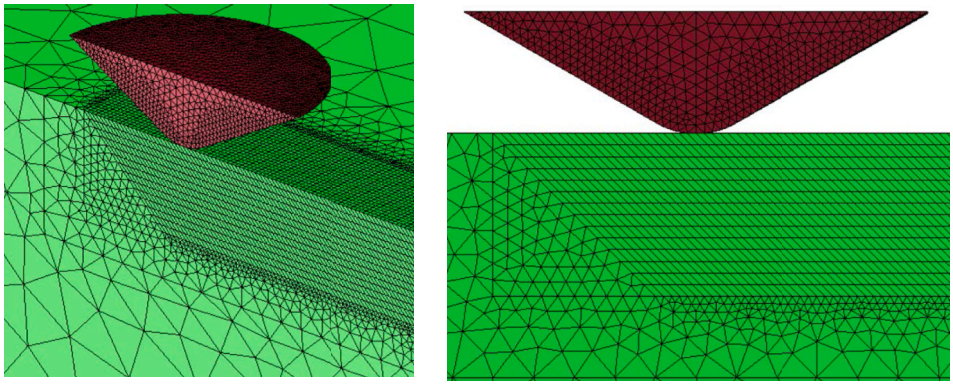

(a) Isometric view. (b) Side view.

Fig. 4. Solution domain: scratch area, initial position.

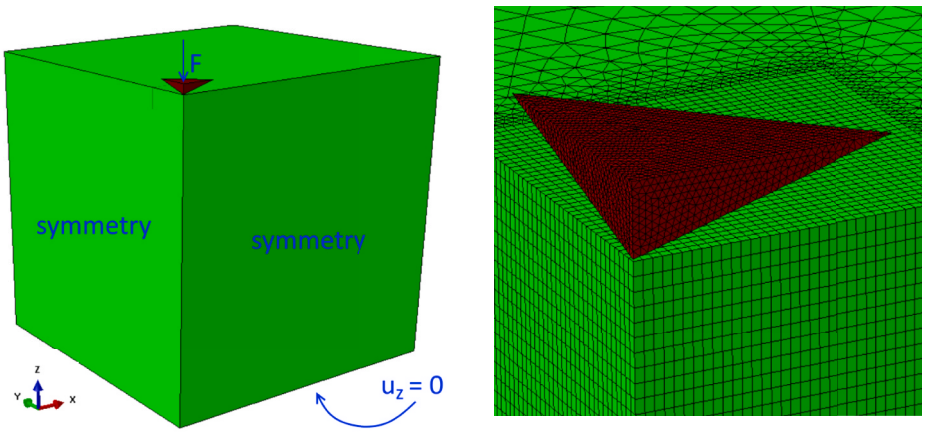

(a) Solution domain. (b) Mesh in the indenter-sample contact area.

Fig. 5. Solution domain for the microindentation tests with Vicker's indenter.

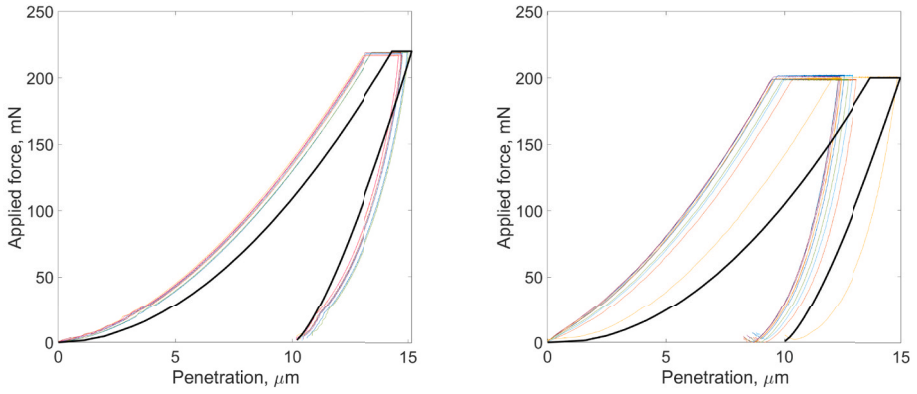

(a) 100 mN/min (b) 1000 mN/min

Fig. 6. Applied force versus penetration depth for the Vicker's indentation test: experimental (colored lines) and numerical results (black solid lines).

performed to determine the optimal HDPE sample size and mesh size.

The contact area in HDPE sample was meshed by linear brick elements with reduced integration. The characteristic size of elements is 0.0025 mm, they were elongated in the vertical direction with aspect ratio 2:1:1. Outside the contact area, linear tetrahedral and brick elements of size from 0.0025 mm to 0.1 mm were used. The indenter was also meshed by tetrahedral linear elements.

Solution in Abaqus/Standard was performed in five nonlinear steps. First, the indenter performed a small vertical movement towards the HDPE sample to ensure the initial contact and begin the process of penetration. Next, the force applied to the indenter increased steadily from 0 to 220 mN (at a rate of 100 mN/min) or 200 mN (at 1000 mN/min), which led to the indentation process. After that, the force remained constant for 120 s, and then the indenter moved out of the

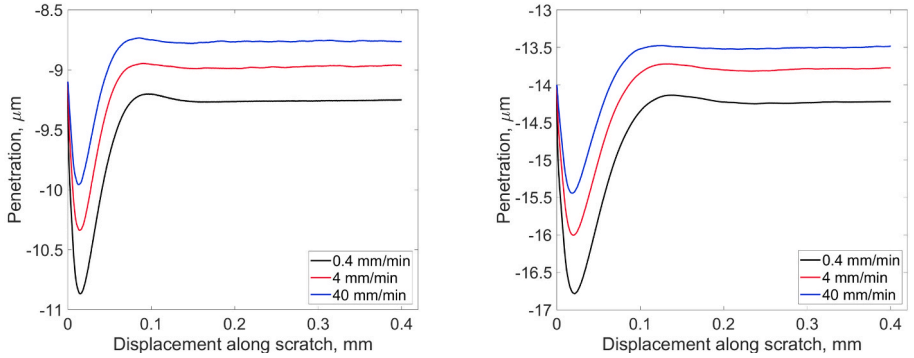

(a) loading 0.1 N (b) loading 0.2 N

Fig. 7. Vertical displacement (penetration) of the scratching indenter versus its horizontal displacement along the scratching direction for different loadings and scratch velocities. The indenter moves from 0 (initial contact) to 0.4 mm (total scratch length).

material with a decrease in force from maximum to zero. The relaxation process happened at the final step.

4. Results

4.1. Indentation tests

The results of the real indentation tests and their numerical simulations are presented in Fig. 6. The local regression smoothing method with window size factor 0.01 was applied to reduce fluctuations in the experimental data. The effect of loading rate can be observed on the results, more stable values were obtained with slower loading rate and higher deviation on the faster approach. The dotted curves of different colors represent separate experiments whereas the black solid lines are the numerical results calculated using the material parameters from Table 1. Note that the maximal loading for the rate 100 mN/min is 220 mN, and for the rate 1000 mN/min is 200 mN.

As it has been already mentioned above in Section 3.1, the results of indentation tests were used to further adjust the material parameters tuned with the aid of tensile experiments. Due to specifics of the

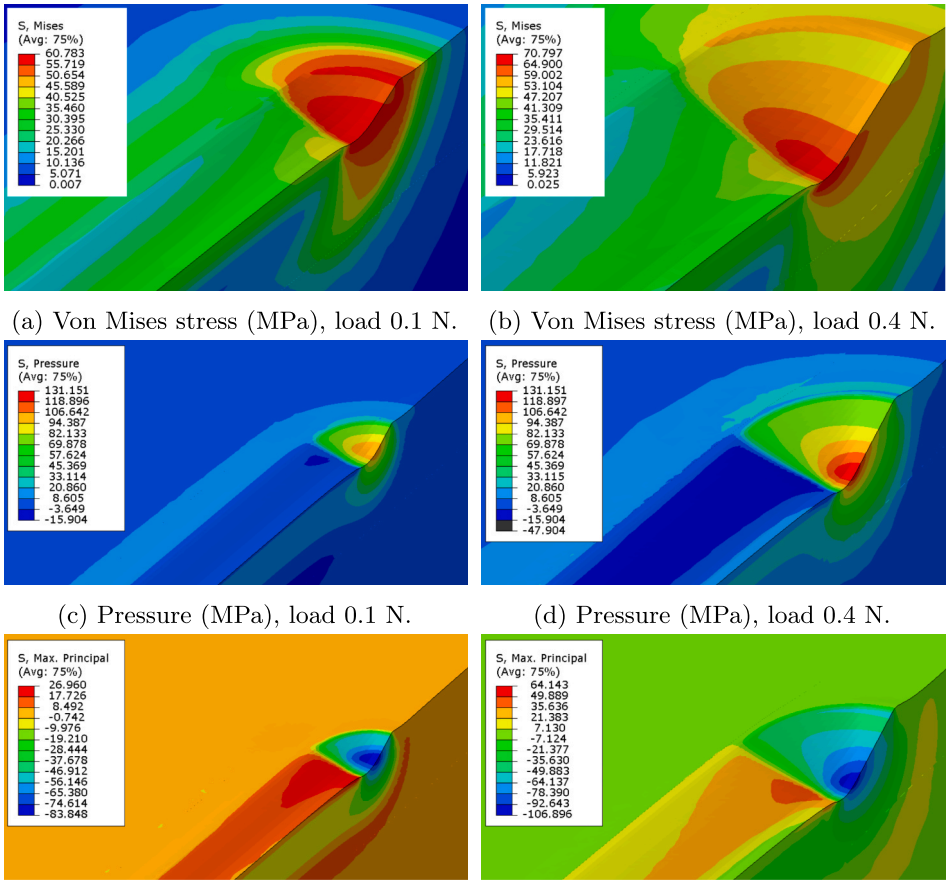

(a) Von Mises stress (MPa), load 0.1 N. (b) Von Mises stress (MPa), load 0.4 N.

(c) Pressure (MPa), load 0.1 N. (d) Pressure (MPa), load 0.4 N.

(e) Maximal principal stress (MPa), load 0.1 N. (f) Maximal principal stress (MPa), load 0.4 N.

Fig. 8. Stress resultants fields in scratch area at velocity 4 mm/min.

measurements during the indentation tests with small loadings, it is difficult to establish exactly the moment when the penetration starts. This can cause some inexactness in the penetration values, especially at the start of the process. From the other hand, the more important parts are not drastically affected, such as the viscous penetration "plateau" during the loading pause, amount of residual plastic penetration depth after relaxation, and patterns of loading and unloading.

Comparing the black curve of the numerical results in Fig. 6a to the dotted lines of the experimental data, one can conclude that the numerical calculations demonstrate, in general, quite good correlation. With almost equal maximal penetration, the simulation shows slightly faster penetration during the loading step and smaller amount of viscous deformations. The similarity of penetration depth after the unloading step reveals that the amount of plastic deformations is nearly correct in the model.

Regarding the loading rate of 1000 mN/min in Fig. 6b, the numerical model shows, on the whole, the correct tendency towards strain rate dependency: greater penetration during the pause in loading (comparing to the case of 100 mN/min) and slightly lower penetration during loading step. However, the material model does not allow to properly simulate the loading process at this rate, and this leads to a difference in the entire indentation process modeling.

4.2. Scratch tests

For numerical simulations of the scratching process, with analogy to the real experiments, the two constant normal concentrated forces of 0.1 N and 0.2 N were applied as well as three scratching velocities 0.4 mm/min, 4 mm/min and 40 mm/min for each load. In addition, a case of 0.4 N force at 4 mm/min was used for some comparisons. Fig. 7 depicts the modeled penetration depth versus displacement of the tip along the scratch. In the real experiment, the scratch length is 5 mm, but as it can be seen from simulations, the initial perturbations (deeper penetration in the beginning of the graphs) fade quite fast for considered cases. In the steady-state regime, the penetration depth is practically constant. The same can be stated for the other resultants like strains and stresses. So, the simulations were restricted by the scratches of 0.4 mm since the longer ones are simply not needed.

The stress resultants fields used for analysis of the scratching process are plotted in Fig. 8. For better visualization, the scratching tip currently located in the top-right area of the pictures (the most deformed area of the scratch groove) was removed. One can see that the range of Von Mises stresses in Fig. 8a and b is almost equal for two different loads 0.1 N and 0.4 N as well as for different scratch velocities (not shown here). This can be explained by the non-linear dependence of stresses on the applied load due to a conical shape of the tip with obtuse conical angle. The higher the applied load is – the larger area is involved in the contact. This is especially notable in the pressure distribution shown in Fig. 8c and d (note the same scale): the load is 4 times bigger (from 0.1 to 0.4 N), but the contact area is roughly 5 times larger and maximal pressure is only 20% higher.

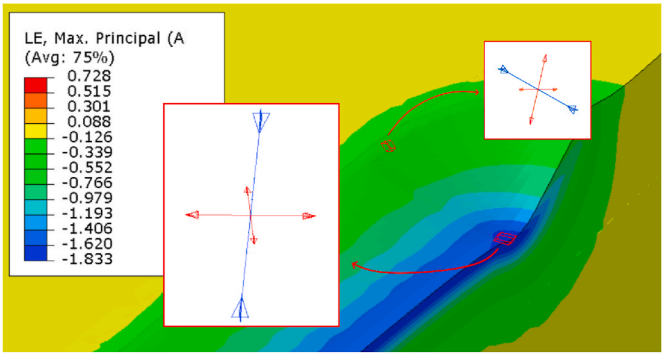

Fig. 10. Principal strains in the scratch bottom and shoulder. The red (tension) and blue (compression) arrows denote the principal strain directions, their lengths are proportional to strain values.

Comparing the Von Mises stress and pressure plots, one can see that the Von Mises stresses are maximal right under the tip whereas the pressure maximum is located ahead of the tip.

The maximal principal stresses are positive (stretching) behind the tip and negative (compression) ahead of the tip (Fig. 8e and f). This explains the maximal Von Mises stresses below the tip, as there the maximal principal stress changes rapidly. In contrast to Von Mises stresses, the maximal principal stress values are sensitive to the applied load, showing 2–3 times larger tensile stresses for 0.4 N load compared to 0.1 N.

Strains, as expected, depend on the load level. As observed in Fig. 9, the maximal principal strains are two times larger (in absolute value) for 0.4 N load comparing to 0.1 N. Strains are very large in a thin layer at the bottom, and moderate in the thin surface layer in the scratch groove.

Fig. 10 depicts the principal strains and their directions for two elements (highlighted in the figure), in the bottom of the scratch and in the topmost point of the scratch shoulder. Blue and red arrows represent, correspondingly, compression and tension. The length of the arrows is proportional to the strain values. One can see that at the bottom of the scratch, where the compression strains are the highest, two other principal strains are high in stretching, a consequence of Poisson's effect. In the shoulder area of the scratch the situation is more complex – the material is affected by simultaneous moderate stretching and compression in two different directions and low stretching in third direction.

Fig. 11 shows the strain rates under the moving tip. Briscoe et al. define an effective scratch strain rate for a conical tip by $\varepsilon_S = v/d$, where v is the scratch velocity and d is the scratch width [42]. The value of ε_S is approximately 0.3 and 30 s^{-1} for velocities 0.4 and 40 mm/min, respectively, in good agreement with the strain rates on the advancing front in Fig. 11. However, the material entering contact with the tip experiences strain rates that are almost two times higher. Furthermore, positive strain rates can be observed behind the tip where both stretching in scratch direction and elastic recovery from compression take place. The dependency of strain rate on the scratch velocity shows the importance of correct rate dependency in the material model.

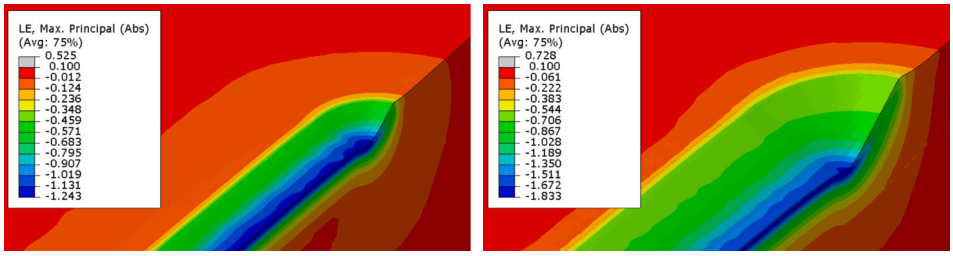

(a) Load 0.1 N. (b) Load 0.4 N.

Fig. 9. Maximal principal logarithmic strain.

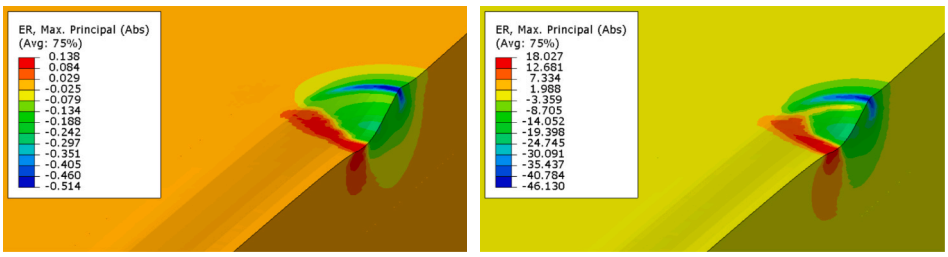

(a) Velocity 0.4 mm/min. (b) Velocity 40 mm/min.

Fig. 11. Maximal (absolute) principal strain rate (s^{-1}) for load 0.1 N and different scratch velocities.

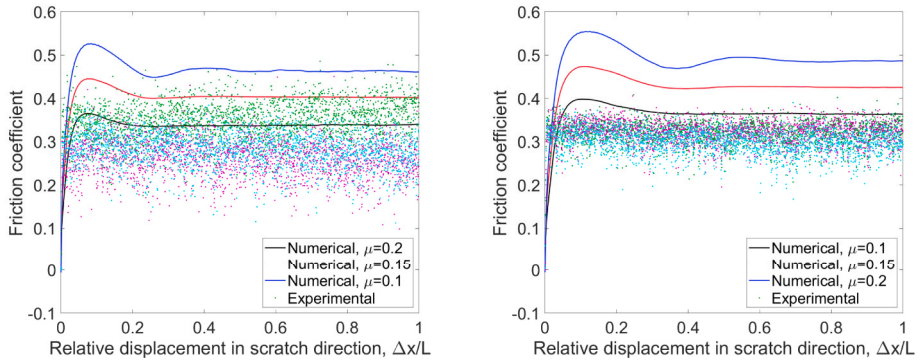

(a) Loading 0.1 N. (b) Loading 0.2 N.

Fig. 12. Experimental and numerical friction coefficient values (ploughing + adhesive) versus relative displacements of the tip along scratch direction x; L is total scratch length, $L = 5$ mm in experiments and 0.4 mm for numerical calculations. Scratch velocity 4 mm/min.

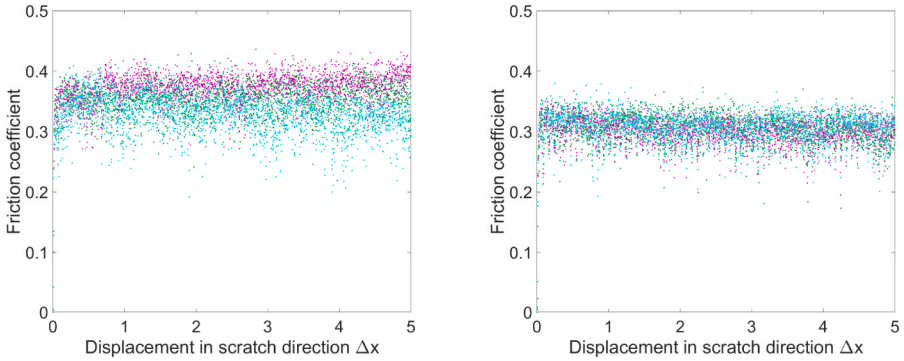

(a) f-Al_2O_3 composite. (b) γ-Al_2O_3 composite.

Fig. 13. Experimental values of friction coefficient (ploughing + adhesive) versus displacement of the tip along scratch direction x. Scratch velocity 4 mm/min, loading 0.2 N.

4.3. Friction

The total friction coefficient observed in a scratch test is a sum of adhesive and ploughing contributions. By numerical simulations, the values for adhesive and ploughing coefficients can be determined by adjusting the adhesive friction in order to match the total friction with the experimental result. The dots in Fig. 12 show friction values measured during experiments for loadings of 0.1 N and 0.2 N, different colors depict different experimental runs. Although some noise is present in the data, we can estimate the total coefficient of friction around 0.3. This value is slightly larger for the higher loading (0.2 N) with lower standard deviation (0.03) due to more significant ploughing effect than with 0.1 N loading, standard deviation of 0.05.

The solid curves in Fig. 12 show the total friction coefficient in simulations with different coefficients of adhesive friction $\mu = 0.1, 0.15, 0.2$. Note that for the sake of convenience, the horizontal axis represents a dimensionless relative displacement in order to show both the experimental scratches and the much shorter numerical scratch in the same plot. The adhesive friction coefficient $\mu = 0.1$ give a reasonable agreement with the experiments, and is therefore used in our calculations. In the literature, the values for the adhesion friction coefficient between HDPE and diamond vary significantly, the value chosen here is at the lower end of the range.

For the sake of completeness, we publish the measured friction data for the nanocomposites being considered (Fig. 13). One can note that for γ-Al_2O_3 composite the friction coefficient is roughly equal to its value for

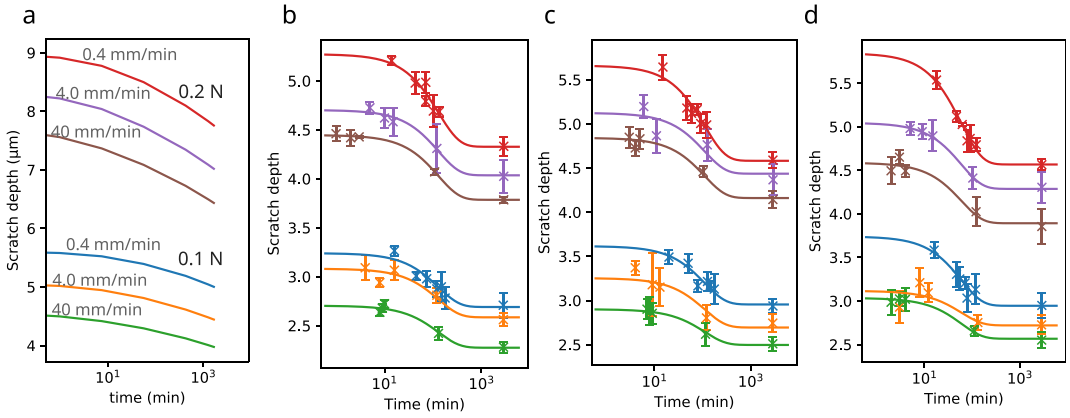

Fig. 14. The relaxation of the scratch groove depth in (a) simulation and (b) experimental values for neat HDPE, experimental values for (c) f-Al_2O_3 composite and (d) γ-Al_2O_3 composite, as a function of relaxation time.

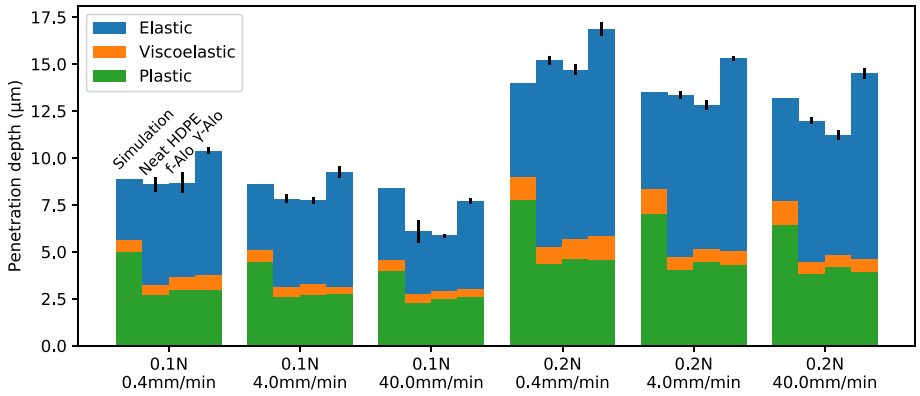

Fig. 15. The decomposition of the penetration depth into elastic, viscoelastic and plastic components for neat HDPE (simulation and experiment) and alumina composites.

neat HDPE (slightly higher than 0.3) with standard deviation of 0.06, whereas for f-Al_2O_3 composite the friction is notably higher (around 0.35, with standard deviation of 0.04).

4.4. Penetration depth and recovery in neat polymer and composites

Fig. 14 shows the relaxation of the scratch groove depth as a function of time for the simulations and experiments. The experimental data seem to follow an exponential relaxation behavior consistent with simple viscoelasticity. A certain portion of the groove depth is subject to viscoelastic relaxation, while the rest is permanent and can be called plastic depth. On top of the plastic and viscoelastic depth, there is component that recovers as soon the load is removed (not shown in Fig. 14). We refer to it here as elastic for simplicity, although it may have viscoelastic character, just with a very short relaxation time. The total depth d can be written as

$$d = d_{\mathrm{pl}} + d_{\mathrm{ve}}\exp(-\lambda(t-t_0)) + d_{\mathrm{el}}\delta(t-t_0) \tag{4.4}$$

where the three terms on the right hand side are the plastic, viscoelastic and elastic contributions, respectively. The relaxation constant is denoted by λ, t_0 is the time of scratching and $\delta(t)$ is the Dirac delta function.

Fitting the function in eq. (4.4) to the experimental data in Fig. 14 yields values for the plastic depth d_{pl} and the initial viscoelastic depth d_{ve}. According to the fit, the relaxation constant λ has the values 0.008, 0.009 and 0.016 min^{-1} for neat HDPE, f-Al_2O_3 and γ-Al_2O_3, respectively. However, it is clear from Fig. 14a that the simulations follow a non-exponential relaxation law that is different from the experiments. The relaxation in the simulation comes from the properties of the Eyring dashpot that gives a viscoplastic nature to the material model. An Eyring dashpot does show linear viscosity at low stresses, which might lead one to think it would relax exponentially. However, the relaxation becomes exceedingly slow before the transition to the linear regime, as a result of which the relationship between stress and relaxation rate always remains non-linear. Therefore, the Eyring dashpot is not suitable to reproduce the exponential relaxation found in the experiments.

Based on the total penetration depth of the indenter and the data in the relaxation plot (Fig. 14), we can break down the total penetration depth into elastic, viscoelastic and plastic components. The results are shown in Fig. 15. It should be noted that the amount of viscoelastic penetration is not well described in the case of the simulation as discussed above; therefore, for the purposes of Fig. 15, we defined the amount of viscoelastic relaxation as the amount of relaxation that occurs in 2000 min, which reflects the experimentally accessible time scale.

From Fig. 15, one can see that the penetration depth in simulation is generally in the correct range, but fails to reproduce the experimental results in certain aspects. First, the amount of plastic depth is much larger than in experiment, while the amount of elastic depth is smaller. Furthermore, the scratch speed dependence of the simulation is much

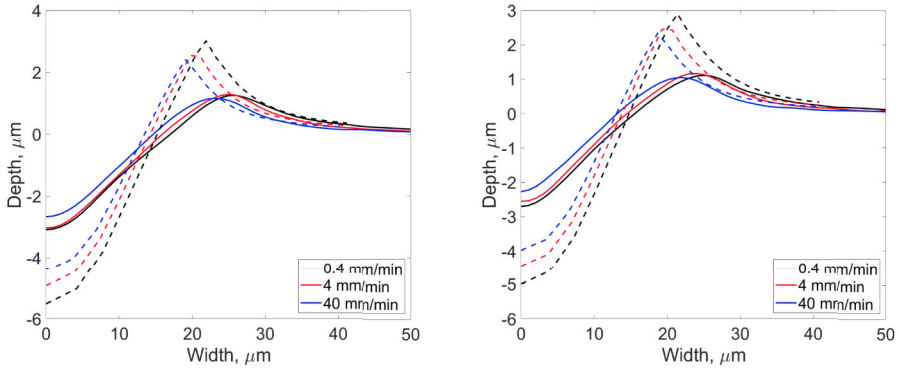

Fig. 16. Scratch half-profiles: experimental (solid lines) and numerical (dashed) results for neat HDPE. Loading 0.1 N.

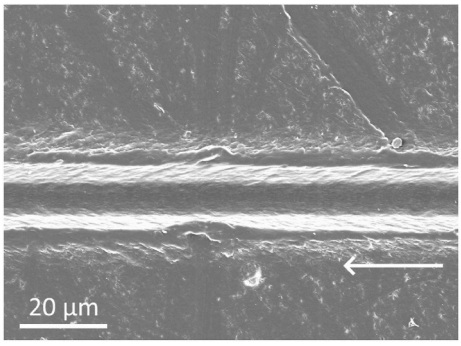

Fig. 17. FIB-SEM image of the scratch groove in neat HDPE (loading 0.2 N). The white arrow shows the scratching direction.

weaker than in experiments. Upon close inspection, the difference does not come from the plastic part (the rate dependency of the yield stress was calibrated with tensile data, after all) but from the elastic part. In simulation, the elastic depth slightly increases with increasing scratch speed — this is expected, as the increasing deformation rate leads to a higher yield stress. However, in experiments, a higher scratch speed causes an opposite effect. This is likely a result of a viscoelastic character present in the elastic part leading to a rate dependency in the effective compressive modulus. This viscoelasticity likely has a relaxation time in the range of seconds, instead of hours like the term governed by λ in eq. (4.4).

In Fig. 16 experimental and numerical scratch profiles are plotted both soon after scratching and two days later for a loading of 0.1 N. One can see that in the recovery of both the scratch depth and shoulder height is much greater in the experiment than simulation, in accordance with Fig. 15.

4.5. Microscopy images

The FIB-SEM image of the scratch groove in neat HDPE is presented in Fig. 17, for illustrative purposes.

The FIB-SEM images of the undeformed materials are presented in Fig. 18. As one can see, there are only few voids in the neat HDPE (they are marked with white arrows in 18a), whereas the same size cross-sectional image of fumed Al_2O_3 composite (see 18b) contains much more cavities. This porosity can be possibly explained by air bubbles admixing into the material during the nanocomposite preparation.

The FIB-SEM images of fumed alumina composite taken after the scratching and relaxation (more than 48 h) are depicted in Fig. 19. One can note that there is no visible cavities in the bottom of the scratch groove, suggesting that deformations under the scratch tip are large enough to cause void closure. In the shoulder region, the number of voids is relatively large and comparable to that in the undeformed composite material, indicating that void closure does not occur in the shoulder where the deformations are smaller than in the bottom.

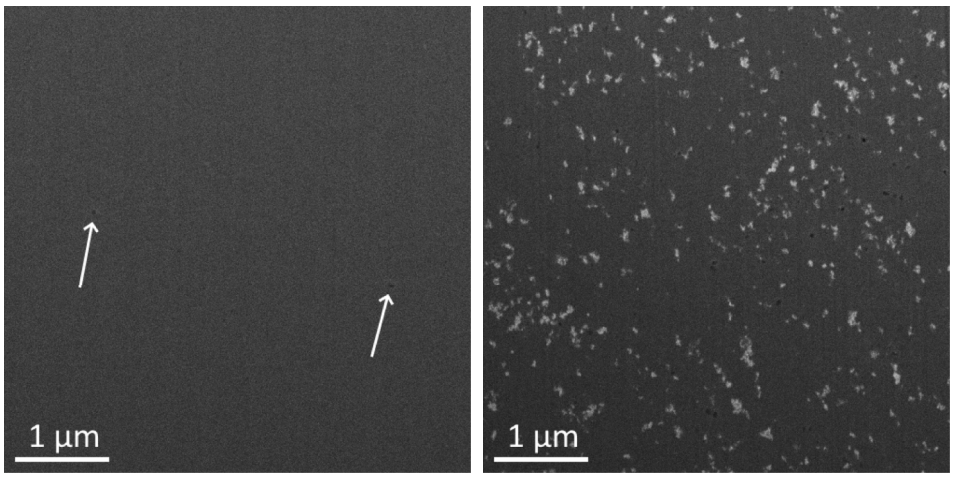

Fig. 18. FIB-SEM images of undeformed material.

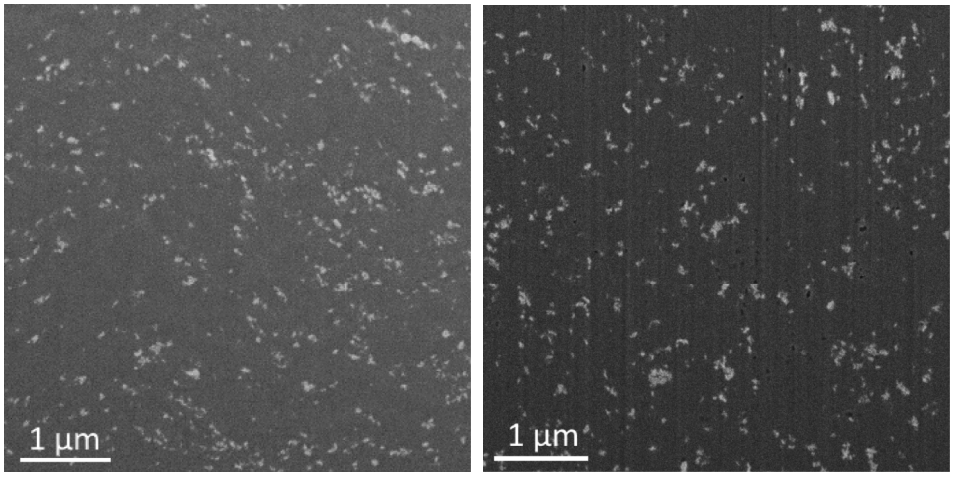

(a) Scratch bottom (b) Scratch shoulder

Fig. 19. FIB-SEM images of deformed f-Al_2O_3 composite.

5. Discussion

5.1. Neat HDPE

During the scratching process, large contact forces in the relatively small area under the scratch tip cause high local tensile deformations in soft materials such as HDPE. This raises some challenges for finite element analysis due to large distortions of the elements at the surface. However, such problems are not usually discussed in the literature devoted to simulations of polymers scratching. In order to improve the convergence of the solution process and the result in general, we apply some numerical tricks such as element elongation and initial distortion described in Section 3.2.1.

A rheological model with viscoplastic yield behavior and network hardening based on the eight chain model [37] was applied for the first time for numerical simulations of scratching. The number of material parameters was reduced by excluding thermal effects and owing to the simpler rate dependency of HDPE compared to cross-linked polyethylene. Material properties were calibrated with the aid of tensile and indentation experiments. The adhesive friction coefficient in numerical model was also calibrated with the aid of data measured in scratching experiments.

Comparison of the total penetration depths shows relatively good agreement between the experimental and numerical tests for most loads and scratch velocities considered, as seen in Fig. 15. However, the rate dependency, a crucial factor not always properly considered in finite element models of scratching, is not entirely correctly captured in the model, as the simulated penetration shows much weaker scratch velocity dependency than the experiments. While the plastic component seems to show a more or less correct rate dependency, there is discrepancy in the elastic component, which has a strong rate dependency in experiments but not in the model. Furthermore, the model overestimates the amount of permanent plastic deformation and underestimates the recovery. The problem likely lies in the fact that the model, whose small deformation behavior is governed by an elastic spring coupled with an Eyring dashpot, does not properly reproduce the viscoelastic character of the recovery found in polymers. The strain recovery behavior of the Eyring dashpot is also quantitatively different than the slow time scale viscoelastic recovery found in experiments, but this difference is of minor consequence as the slowly recovering part is only a small fraction of the total penetration.

Scratch modeling of highly deformable polymers is a challenging task as it involves not only large deformations under the scratch tip, but also sensitive to small deformations and strain recovery, since a large volume around the contact experiences moderate stresses. Moreover, rate sensitivity should be correctly included in both aspects. The same challenges concern indentation simulations (see Fig. 6). The present physically motivated material model formulation works well in reproducing large deformation behavior, but is overly simplified in its treatment of small deformation and recovery effects. A large number of studies have been published that aim to accurately reproduce the small deformation and cycling behavior of polymers by phenomenological models [43–47], but we are not aware of any that would generalize to three dimensions and large deformations, which would be needed for the finite element analysis of scratching.

5.2. HDPE-alumina nanocomposites

Analysis of the penetration depths (the third and fourth bars for each of the cases in Fig. 15) allows to conclude that the fillers slightly decrease elastic penetration for fumed alumina composite but greatly increase it for the gamma alumina composite. The most likely reason for this is the effect of the fillers on the elastic modulus. Penetration data suggests that the gamma-alumina composite has a lot lower modulus than the neat polymer. This is in agreement with the results obtained in Ref. [16]. Furthermore, the nanocomposites seem to show slightly more non-recoverable penetration than the neat polymer. Interestingly, the fumed Al_2O_3 composite had a slightly larger total coefficient of friction than the neat polymer (Figs. 12 and 13). A possible explanation is a larger proportion of dissipative (plastic and viscoelastic) deformation in the nanocomposite, suggested by the slightly larger proportion of plastic and viscoelastic penetration shown in Fig. 15. The γ-Al_2O_3 composite, which had a markedly large elastic penetration, had the same friction coefficient as the neat polymer.

Separate scratch simulations for composite materials were not within the scope of this study. However, comparison between the penetration depths (Fig. 15) shows that the differences between the neat polymer and composites are subtle apart from the difference in the elastic modulus in the case of gamma alumina. To properly understand the effect of the filler particles on the macroscopic behavior of a nanocomposite, a representative volume element based micromechanical homogenization study could be performed [48]. However, on a phenomenological level, the considered material model can be fitted to represent the composites using data from e.g. tensile tests.

The FIB-SEM images in Figs. 18 and 19 revealed porosity in fumed Al_2O_3 composite, whereas neat HDPE only showed a few isolated voids. Although we do not have data available for the gamma alumina composite to make a more generalized conclusion, we note that the presence

of cavities is expected to affect the behavior of the material and is something to consider during fabrication and modeling. FIB-SEM micrographs from the bottom of the groove show that the voids are eliminated during the large compressive deformations during the contact with the tip, as seen in Fig. 19a. However, at the shoulder, where less dramatic deformation takes place (see Fig. 10), evidence of void elimination was not observed (Fig. 19b).

The nanoparticle (NP) chain-like aggregates seen in the FIB-SEM images are originated from the native dry nanopowder, which is aggregated permanently and cannot be dispersed into smaller clusters. The aggregates are separated by 100–200 nm distances corresponding to the length scale of "ideal" NP dispersion. This is roughly the distance two-three times the diameter of coiled high molecular weight polymer chains, thus enabling the direct NP interactions for the bulk of polymer, while retaining the polymeric melt flow and solid state ductility [22]. The NP aggregates appear unaffected by the large macroscopic deformations in terms of size and shape, suggesting that they are mechanically stable.

6. Conclusion

We used modeling and experimentation to study the scratch behavior of HDPE. Furthermore, we experimentally investigated the effect of nanoparticle fillers on the scratch properties. To the best of our knowledge, the numerical simulation of scratching and indentation processes in high molecular weight HDPI was performed for the first time in the literature. The general aspects of the scratching process were well described by the simulation, and the predicted penetration depth was in reasonable agreement with experiments. However, the great deformability of HDPE combined with its intricate viscoelastic small deformation and recovery behavior makes it a challenge for modeling. We used an elasto-viscoplastic constitutive model that provides a good description of plasticity and hardening. We made an attempt to adequately account the rate dependency, usually omitted in the literature, however, it still has room for improvement in the areas of rate-dependent viscoelastic loading and unloading behavior. More research is needed to develop material models for finite element analysis that correctly capture all the aspects of material performance that come to play during scratching. The nanoparticles fillers had only a minor effect on the scratch behavior, but we did see an increase in the elastic penetration in the case of gamma alumina filler (up to 12%, depending on the scratch velocity and loading), attributable to a decrease in the elastic modulus. This does not affect the friction behavior: the friction coefficients for neat HDPE (0.32 ± 0.05) and gamma alumina composite (0.31 ± 0.06) are close to each other. The friction coefficient for fumed alumina composite is 0.35 ± 0.04, and the difference can be explaned by a larger proportion of dissipative (plastic and viscoelastic) deformation.

Data availability

The raw and processed data required to reproduce the presented findings cannot be shared at this time due to technical and time limitations.

Declaration of competing interest

The authors declare that they have no known competing financial interests or personal relationships that could have appeared to influence the work reported in this paper.

Acknowledgements

This work was supported by the Academy of Finland (Grant No.289255) and VTT Technical Research Centre of Finland Ltd.

References

[1] Janet S.S. Wong, Sue Hung-Jue, Scratch behavior of polymers. Encyclopedia of Polymer Science and Technology, John Wiley & Sons, Inc., Hoboken, NJ, USA, 2004, p. 7.
[2] B.J. Briscoe, S.K. Sinha, Wear of polymers, Proc. IME J. J. Eng. Tribol. 216 (6) (2002) 401–413.
[3] C. Xiang, H.J. Sue, J. Chu, B. Coleman, Scratch behavior and material property relationship in polymers, J. Polym. Sci. B Polym. Phys. 39 (1) (2001) 47–59.
[4] Pinar Kurkcu, Luca Andena, Andrea Pavan, An experimental investigation of the scratch behaviour of polymers: 1. Influence of rate-dependent bulk mechanical properties, Wear 290–291 (2012) 86–93.
[5] A. Dasari, S.J. Duncan, R.D.K. Misra, Micro- and nano-scale deformation processes during scratch damage in high density polyethylene, Mater. Sci. Technol. 19 (2) (2003) 239–243.
[6] N. Guermazi, K. Elleuch, H.F. Ayedi, H. Zahouani, Ph Kapsa, Susceptibility to scratch damage of high density polyethylene coating, Mater. Sci. Eng. 492 (1–2) (2008) 400–406.
[7] F.S.P. Stan, Looijmans, D. Patrick, Anderson, C.A. Lambèrt, van Breemen, Contact mechanics of high-density polyethylene: effect of pre-stretch on the frictional response and the onset of wear, Wear 410– (2018) 9, 411:142–148.
[8] A. Mudaliar, Q. Yuan, R.D.K. Misra, On surface deformation of melt-intercalated polyethylene-clay nanocomposites during scratching, Polym. Eng. Sci. 46 (11) (11 2006) 1625–1634.
[9] Brian B. Johnson, Michael H. Santare, John E. Novotny, Suresh G. Advani, Wear behavior of carbon nanotube/high density polyethylene composites, Mech. Mater. 41 (10) (2009) 1108–1115.
[10] Maija Pöllänen, Sami Pirinen, Mika Suvanto, T. Tuula, Pakkanen. Influence of carbon nanotube-polymeric compatibilizer masterbatches on morphological, thermal, mechanical, and tribological properties of polyethylene, Compos. Sci. Technol. 71 (10) (2011) 1353–1360.
[11] D.B. Stojanović, A. Orlović, M. Zrilić, I. Balać, C.Y. Tang, P.S. Uskoković, R. Aleksić, The effects of functionalization on the thermal and tribo-mechanical behaviors of neat and grafted polyethylene nanocomposites, Polym. Compos. 34 (10) (10 2013) 1710–1719.
[12] M. Tanniru, R.D.K. Misra, K. Berbrand, D. Murphy, The determining role of calcium carbonate on surface deformation during scratching of calcium carbonate-reinforced polyethylene composites, Mater. Sci. Eng. 404 (1–2) (2005) 208–220.
[13] N.L. Surampadi, T.C. Pesacreta, R.D.K. Misra, The determining role of scratch indenter radius on surface deformation of high density polyethylene and calcium carbonate-reinforced composite, Mater. Sci. Eng. 456 (1–2) (2007) 218–229.
[14] Valeria Pettarin, Maria Jose Churruca, Dávid Felhös, Joseph Karger-Kocsis, Patricia Maria Frontini, Changes in tribological performance of high molecular weight high density polyethylene induced by the addition of molybdenum disulphide particles, Wear 269 (1–2) (2010) 31–45.
[15] Songbo Xu, X.W. Tangpong, Review: tribological behavior of polyethylene-based nanocomposites, J. Mater. Sci. 48 (2) (1 2013) 578–597.
[16] Jani Pelto, Tuukka Verho, Helena Ronkainen, Kimmo Kaunisto, Jarkko Metsäjoki, Jani Seitsonen, and Mikko Karttunen. Matrix morphology and the particle dispersion in HDPE nanocomposites with enhanced wear resistance. Polym. Test., 77:105897, 8 2019.
[17] D. Liu, A.M. Pourrahimi, R.T. Olsson, M.S. Hedenqvist, U.W. Gedde, Influence of nanoparticle surface treatment on particle dispersion and interfacial adhesion in low-density polyethylene/aluminium oxide nanocomposites, Eur. Polym. J. 66 (2015) 67–77.
[18] D. Liu, L.K.H. Pallon, A.M. Pourrahimi, P. Zhang, A. Diaz, M. Holler, K. Schneider, R.T. Olsson, M.S. Hedenqvist, S. Yu, U.W. Gedde, Cavitation in strained polyethylene/aluminium oxide nanocomposites, Eur. Polym. J. 87 (255–265) (2017).
[19] D. Liu, A.T. Hoang, A.M. Pourrahimi, L.K. H Pallon, F. Nilsson, S.M. Gubanski, R. T. Olsson, M.S. Hedenqvist, U.W. Gedde, Influence of nanoparticle surface coating on electrical conductivity of LDPE/Al2O3 nanocomposites for HVDC cable insulations, IEEE Trans. Dielectr. Electr. Insul. 24 (3) (6 2017) 1396–1404.
[20] Amir Masoud Pourrahimi, Richard T. Olsson, Mikael S. Hedenqvist, Nanocomposites: the role of interfaces in polyethylene/metal-oxide nanocomposites for ultrahigh-voltage insulating materials, Adv. Mater. 4/2018). Advanced Materials 30 (4) (2018), 1870025.
[21] C.W. Reed, The chemistry and physics of the interface region and functionalization, in: Dielectric Polymer Nanocomposites, 95–131, Springer US, Boston, MA, 2010.
[22] Jani Pelto, Vuokko Heino, Mikko Karttunen, Ilkka Rytöluoto, and Helena Ronkainen. Tribological performance of high density polyethylene (HDPE) composites with low nanofiller loading. Wear, 460–461:203451, 2020.
[23] J. L Bucaille, E. Felder, G. Hochstetter, Mechanical analysis of the scratch test on elastic and perfectly plastic materials with the three-dimensional finite element modeling, Wear 249 (5–6) (2001) 422–432.
[24] Eric Felder, Jean Luc Bucaille, Mechanical analysis of the scratching of metals and polymers with conical indenters at moderate and large strains, Tribol. Int. 39 (2) (2006) 70–87.
[25] Fredrik Wredenberg, Per-Lennart Larsson, On the numerics and correlation of scratch testing, J. Mech. Mater. Struct. 2 (3) (5 2007) 573–594.
[26] Mohammad Motaher Hossain, Han Jiang, Sue Hung-Jue, Effect of constitutive behavior on scratch visibility resistance of polymers—A finite element method parametric study, Wear 270 (11–12) (2011) 751–759.
[27] Mohammad Motaher Hossain, Rolf Minkwitz, Piyada Charoensirisomboon, Jue Sue Hung, Quantitative modeling of scratch-induced deformation in amorphous polymers, Polymer 55 (23) (2014) 6152–6166.

[28] Mohammad Motaher Hossain, Shuang Xiao, Sue Hung-Jue, Masaya Kotaki, Scratch behavior of multilayer polymeric coating systems, Mater. Des. 128 (143–149) (8 2017).
[29] H. Jiang, G.T. Lim, J.N. Reddy, J.D. Whitcomb, H.J. Sue, Finite element method parametric study on scratch behavior of polymers, in: Journal of Polymer Science, Part B: Polymer Physics, 45, John Wiley & Sons, Ltd, 2007, pp. 1435–1447.
[30] Han Jiang, Robert Browning, Jue Sue Hung, Understanding of scratch-induced damage mechanisms in polymers, Polymer 50 (16) (2009) 4056–4065.
[31] H. Pelletier, C. Gauthier, R. Schirrer, Experimental and finite-element analysis of scratches on amorphous polymeric surfaces, Proc. IME J. J. Eng. Tribol. 222 (3) (2008) 221–230.
[32] Hervé Pelletier, Christian Gauthier, Robert Schirrer, Strain and stress fields during scratch tests on amorphous polymers: Influence of the local friction, Tribol. Lett. 32 (2) (2008) 109–116.
[33] Hervé Pelletier, , Anne-Lise Durier, Christian Gauthier, Robert Schirrer, Viscoelastic and elastic–plastic behaviors of amorphous polymeric surfaces during scratch, Tribol. Int. 41 (11) (11 2008) 975–984.
[34] Hervé Pelletier, Christian Gauthier, Robert Schirrer, Influence of the friction coefficient on the contact geometry during scratch onto amorphous polymers, Wear 268 (9–10) (2010) 1157–1169.
[35] N. Aleksy, G. Kermouche, A. Vautrin, J.M. Bergheau, Numerical study of scratch velocity effect on recovery of viscoelastic-viscoplastic solids, Int. J. Mech. Sci. 52 (3) (2010) 455–463.
[36] G. Kermouche, N. Aleksy, J.M. Bergheau, Viscoelastic-viscoplastic modelling of the scratch response of PMMA, Advances in Materials Science and Engineering 1–10 (2013) 3.
[37] Joakim Johnsen, Arild Holm Clausen, Frode Grytten, Benallal Ahmed, Odd Sture Hopperstad, A thermo-elasto-viscoplastic constitutive model for polymers, J. Mech. Phys. Solid. 124 (3 2019) 681–701.
[38] Marc J.W. Kanters, Klaas Remerie, Leon E. Govaert, A new protocol for accelerated screening of long-term plasticity-controlled failure of polyethylene pipe grades, Polym. Eng. Sci. 56 (6) (6 2016) 676–688.
[39] R. Hiss, S. Hobeika, C. Lynn, G. Strobl, Network stretching, slip processes, and fragmentation of crystallites during uniaxial drawing of polyethylene and related copolymers. A comparative study, Macromolecules 32 (13) (1999) 4390–4403.
[40] E.N. Brown, R.B. Willms, G.T. Gray, P.J. Rae, C.M. Cady, K.S. Vecchio, J. Flowers, M.Y. Martinez, Influence of molecular conformation on the constitutive response of polyethylene: a comparison of HDPE, UHMWPE, and PEX, Exp. Mech. 47 (3) (5 2007) 381–393.
[41] G.T. Lim, M.H. Wong, J.N. Reddy, H.J. Sue, An integrated approach towards the study of scratch damage of polymer, J. Coating Technol. Res. 2 (5) (1 2005) 361–369.
[42] Brian J. Briscoe, Enrico Pelillo, Sujeet K. Sinha, Scratch hardness and deformation maps for polycarbonate and polyethylene, Polym. Eng. Sci. 36 (24) (12 1996) 2996–3005.
[43] Chuntao Zhang, Ian D. Moore, Nonlinear mechanical response of high density polyethylene. Part II: Uniaxial constitutive modeling, Polym. Eng. Sci. 37 (2) (2 1997) 414–420.
[44] A.D. Drozdov, J.deC. Christiansen, Cyclic viscoplasticity of high-density polyethylene: Experiments and modeling, Comput. Mater. Sci. 39 (2) (2007) 465–480.
[45] J.S. Bergström, S.M. Kurtz, C.M. Rimnac, A.A. Edidin, Constitutive modeling of ultra-high molecular weight polyethylene under large-deformation and cyclic loading conditions, Biomaterials 23 (11) (2002) 2329–2343.
[46] Necmi Dusunceli, U. Ozgen, Colak. High density polyethylene (HDPE): experiments and modeling, Mech. Time-Dependent Mater. 10 (4) (7 2007) 331–345.
[47] Elhem Ghorbel. A viscoplastic constitutive model for polymeric materials. Int. J. Plast., 24(11):2032–2058, 11 2008.
[48] Swantje Bargmann, Benjamin Klusemann, Jürgen Markmann, Jan Eike Schnabel, Konrad Schneider, Celal Soyarslan, Wilmers Jana, Generation of 3D representative volume elements for heterogeneous materials: A review, Prog. Mater. Sci. 96 (2018) 322–384.